

# UC Berkeley

## UC Berkeley Previously Published Works

### Title

The presence and role of the intermediary CO reservoir in heterogeneous electroreduction of CO<sub>2</sub>

### Permalink

<https://escholarship.org/uc/item/0v40t68z>

### Journal

Proceedings of the National Academy of Sciences of the United States of America, 119(18)

### ISSN

0027-8424

### Authors

Louisia, Sheena  
Kim, Dohyung  
Li, Yifan  
[et al.](#)

### Publication Date

2022-05-03

### DOI

10.1073/pnas.2201922119

Peer reviewed

# The presence and role of the intermediary CO reservoir in heterogeneous electroreduction of CO<sub>2</sub>

Sheena Louisa<sup>a,b,†</sup>, Dohyung Kim<sup>a,b,c,†</sup>, Yifan Li<sup>a,b</sup>, Mengyu Gao<sup>c</sup>, Sunmoon Yu<sup>b,c</sup>, Inwhan Roh<sup>a,b</sup>, Peidong Yang<sup>a,b,c,d\*</sup>

† denotes equal contribution

<sup>a</sup>Department of Chemistry, University of California, Berkeley, CA, USA.

<sup>b</sup>Chemical Sciences Division, Lawrence Berkeley National Laboratory, Berkeley, CA, USA.

<sup>c</sup>Department of Materials Science and Engineering, University of California, Berkeley, CA, USA.

<sup>d</sup>Kavli Energy NanoScience Institute, Berkeley, CA, USA.

Correspondence to: \* Peidong Yang

**Email:** p\_yang@berkeley.edu

**Author Contributions:** S.L. and D.K. designed the experiments and analyzed data with assistance from Y.L. and M.G.; S.L. performed the experiments with assistance from D.K., Y.L., and I.R.; S.L. carried out the multiphysics simulation with assistance from D.K.; S.L. and M.G. designed and carried out the numerical model. P.Y. supervised the project and experimental design. All authors wrote the manuscript.

**Competing Interest Statement:** Authors declare no competing interests.

**Classification:** Physical Sciences, Chemistry.

**Keywords:** heterogeneous catalysis, electrocatalysis, CO<sub>2</sub> reduction, analytical method.

**This PDF file includes:**

Main Text  
Figures 1 to 4

## **Abstract**

Despite the importance of the microenvironment in heterogeneous electrocatalysis, its role remains unclear due to a lack of suitable characterization techniques. Multi-step reactions like the electroconversion of CO<sub>2</sub> to multicarbons (C<sub>2+</sub>) are especially relevant considering the potential creation of a unique microenvironment as part of the reaction pathway. To elucidate the significance of the microenvironment during CO<sub>2</sub> reduction, we develop on-stream substitution of reactant isotope (OSRI), a new method which relies on the subsequent introduction of CO<sub>2</sub> isotopes. Combining electrolytic experiments with a numerical model, this method reveals the presence of a reservoir of CO molecules concentrated near the catalyst surface that influences C<sub>2+</sub> formation. Application of OSRI on a Cu nanoparticle (NP) ensemble and an electropolished Cu foil demonstrates that a CO monolayer covering the surface does not provide the amount of CO intermediates necessary to facilitate C-C coupling. Specifically, the C<sub>2+</sub> turnover increases only after reaching a density of ~100 CO molecules per surface Cu atom. The Cu NP ensemble satisfies this criterion at an overpotential 100 mV lower than the foil, making it a better candidate for efficient C<sub>2+</sub> formation. Furthermore, given the same reservoir size, the ensemble's intrinsically higher C-C coupling ability is highlighted by the 4-fold higher C<sub>2+</sub> turnover it achieves at a more positive potential. The OSRI method provides an improved understanding of how the presence of CO intermediates in the microenvironment impacts C<sub>2+</sub> formation during the electroreduction of CO<sub>2</sub> on Cu surfaces.

## **Significance Statement**

The electroconversion of CO<sub>2</sub> to value-added products is a promising path to sustainable fuels and chemicals. However, the microenvironment that is created during CO<sub>2</sub> electroreduction near the surface of heterogeneous Cu electrocatalysts remains unknown. Its understanding can lead to the development of ways to improve activity and selectivity towards multicarbon products. This work presents a new method called on-stream substitution of reactant isotope that provides quantitative information of the CO intermediate species present on Cu surfaces during electrolysis. An intermediary CO reservoir was identified for the first time which contains more CO molecules than typically expected in a surface adsorbed configuration. Its size was shown to be a factor closely associated with the formation of multicarbon products.

## Main Text

### Introduction

Powering the conversion of small molecules into value-added products using renewable electricity is a promising approach to achieve sustainable production of fuels and chemicals.<sup>1-3</sup> The field of electrocatalysis has been moving towards this goal but remains hampered by activity and selectivity challenges. A molecular-level understanding of reactions is required to overcome these difficulties. More importantly, it should involve a thorough consideration of all factors that influence electrochemical conversion at heterogeneous surfaces. Previous studies have suggested that environmental aspects beyond the surface active site may be as critical for facilitating electrocatalytic reactions.<sup>4,5</sup>

Studies in heterogeneous electrocatalysis have largely focused on controlling the active sites and understanding how it influences reaction pathways through techniques such as surface spectroscopy (e.g., *in situ* Raman and IR spectroscopy) combined with theory.<sup>6-8</sup> However, locally confined environments also play a critical role in mediating reactions as demonstrated in other fields of catalysis. For example, in biocatalysis and homogeneous catalysis, the role of the microenvironment and the secondary coordination sphere have been widely investigated, respectively.<sup>9-14</sup> The high selectivity achieved by bio- and molecular catalysts has often been associated with the characteristics of such regimes. Likewise, understanding the influence of a microenvironment in the context of heterogeneous electrocatalysis is necessary to gain better control of reactions. It is expected that the microenvironment created near a catalytically active surface will exhibit specific physicochemical properties that differ from the bulk.

Microenvironment effects may be especially important for the CO<sub>2</sub> reduction reaction (CO<sub>2</sub>RR), particularly on Cu catalysts where a variety of value-added, higher-order products (e.g., ethylene, ethanol) are generated.<sup>15</sup> Up to now, probing key surface intermediates using surface spectroscopy coupled with theoretical calculations has led to the consensus that \*CO is necessary for the formation of multicarbons (C<sub>2+</sub>).<sup>16-18</sup> Further investigation has revealed the importance of its binding mode (i.e., \*CO<sub>atop</sub> or \*CO<sub>bridge</sub>) in determining CO<sub>2</sub>RR selectivity.<sup>19-21</sup> Other studies have reported high \*CO coverage leading to C-C coupling necessary for C<sub>2+</sub> formation.<sup>22,23</sup> However, beyond the surface bound \*CO, recent findings suggest the presence of near-surface CO species during CO<sub>2</sub> electroreduction relevant to C<sub>2+</sub> formation.<sup>24-27</sup> Furthermore, structural modifications presumed to affect the environment surrounding catalysts have been shown to improve C<sub>2+</sub> selectivity.<sup>20,28-30</sup> Considering its critical influence, an in-depth characterization of the microenvironment under CO<sub>2</sub> electroreduction conditions is needed.

However, the characteristics of the microenvironment remain elusive due to the lack of suitable techniques. Despite the insights acquired into surface species present during the reaction, the use of surface spectroscopy has been limited to analytes present within a few nanometers from the surface.<sup>31,32</sup> Vibrational spectroscopy methods, such as Raman or FTIR, are also constrained to rely on surface enhancing effects to overcome the signal loss associated with the electrolyte.<sup>33,34</sup> Additionally, the enhancement decays rapidly away from the surface (inversely proportional to the cube of the distance), exclusively favoring surface bound species.<sup>35-37</sup> At high catalytic rates, optical interference from product bubble formation limits the use of such techniques under catalytically relevant *operando* conditions.<sup>26,38</sup> Overall, the limitations of surface vibrational spectroscopy prevent it from understanding the microenvironment during electrochemical reactions on heterogeneous surfaces.

In this work, we present on-stream substitution of reactant isotope (OSRI) as a new method that can provide insights into the microenvironment near Cu surfaces during CO<sub>2</sub>RR. The OSRI method employs isotopic labeling of the reagent CO<sub>2</sub> in a specific sequence and monitors its transformation to various products. Through the analysis of product isotopic compositions, it reveals the presence of a reservoir of intermediary CO (CO<sub>int</sub>) molecules necessary for C<sub>2+</sub> formation. Applied to two different systems (i.e., Cu nanoparticle (NP) ensemble and polycrystalline Cu foil), a density reaching ~100 CO<sub>int</sub> molecules per surface Cu atom is identified as a common characteristic of the reservoir linked to CO<sub>2</sub> conversion to multicarbons. Furthermore, the intrinsic

C-C coupling ability of a catalyst can be gauged independently from the availability of  $\text{CO}_{\text{int}}$ . Ultimately, we find that the higher  $\text{C}_{2+}$  turnover of the Cu nanoparticles compared against the Cu foil originates from both its ability to form a large  $\text{CO}_{\text{int}}$  reservoir at low overpotentials and its intrinsically higher C-C coupling rate. Through the OSRI method, we identify the importance of a  $\text{CO}_{\text{int}}$  reservoir in the formation of  $\text{C}_{2+}$  over Cu surfaces, which has remained inaccessible thus far from conventional spectroscopic techniques.

## Results and Discussion

The OSRI method starts with the application of a cathodic bias under  $^{12}\text{CO}_{2(\text{g})}$  at a constant flow in aqueous conditions for one hour, followed by a consecutive hour in which  $^{12}\text{CO}_{2(\text{g})}$  feed is substituted with  $^{13}\text{CO}_{2(\text{g})}$  under continued bias (Fig. 1a). The propagation of  $^{13}\text{C}$  can then be tracked across all products generated during electrolysis, using multiple modes of product analysis in both the gas and liquid phase that quantify the isotopic compositions of different products (Fig. 1b). Throughout the two hours, the outlet gas stream is sampled at regular intervals by gas chromatography (GC) for product quantification in real-time. Furthermore, since the products contain a mix of  $^{12}\text{C}$  and  $^{13}\text{C}$  after switching to  $^{13}\text{CO}_{2(\text{g})}$ , the gas products during the second hour are collected in a gas bag (gas bag #1) to study their isotopic composition by gas chromatography-mass spectrometry (GC-MS) (Fig. S1 and Supplementary Text 1). Finally, the liquid products accumulated in the catholyte, as well as the membrane during OSRI, are analyzed using  $^1\text{H}$  and  $^{13}\text{C}$  NMR (Supplementary Texts 2-3). Consequently, both the production rate and the isotopic composition of all formed products can be determined (Methods). Throughout OSRI, the current density and product faradaic efficiencies remained stable (Fig. S9). All potentials are reported on the reversible hydrogen electrode (RHE) scale.

The first catalytic system studied by OSRI was an ensemble of 7 nm Cu nanoparticles (NPs) as reported in previous studies at -0.60 V with CO and  $\text{HCOO}^-$  as  $\text{CO}_2\text{RR}$  products.<sup>39</sup> Because the complete exchange of  $^{13}\text{C}$  for the  $^{12}\text{CO}_{2(\text{aq})}$  is delayed by its equilibration with  $\text{H}^{12}\text{CO}_3^-$  (aq), the overall average of  $^{12}\text{CO}_{2(\text{aq})}$  available should be > 50% (Fig. 1a). As expected, while the  $^{12}\text{C}:^{13}\text{C}$  ratio of  $\text{CO}_{2(\text{g})}$  supplied was 1:1, all products were found with a consistently higher  $^{12}\text{C}$  content (Fig. 2a). The delay of  $\text{CO}_{2(\text{aq})}$  to complete the exchange was theoretically verified through a multiphysics simulation (Methods). Regardless of any  $\text{CO}_{2(\text{aq})}$  consumption taking place at the electrode due to applied potentials, there remains a substantial amount of  $^{12}\text{CO}_{2(\text{aq})}$  available in solution after an hour of purging  $^{13}\text{CO}_{2(\text{g})}$  into a  $^{12}\text{CO}_{2(\text{g})}$  saturated 0.1M  $\text{KH}^{12}\text{CO}_3$  electrolyte (Fig. S10). The multiple equilibria following  $\text{CO}_{2(\text{g})}$  dissolution including  $\text{HCO}_3^-$  (aq) and  $\text{CO}_3^{2-}$  (aq) are responsible for the slow exchange of all  $^{12}\text{C}$  in solution (Supplementary Text 4 and Fig. S11). It should be noted that the colored segments for  $\text{CO}_{2(\text{aq})}$  and the products in Fig. 1a are simply divided to qualitatively depict their average composition during OSRI; however, the true isotopic shift from  $^{12}\text{C}$  to  $^{13}\text{C}$  takes place gradually throughout the two hours as shown in Figs. S10 and S11. Varying the flow rate of  $\text{CO}_{2(\text{g})}$  or the rate of  $\text{CO}_{2(\text{aq})}$  consumption results in changes in the isotopic composition of electrolytically available  $\text{CO}_{2(\text{aq})}$  that are consistent with this analysis (Supplementary Text 5 and Fig. S12).

Although both CO and  $\text{HCOO}^-$  are enriched in  $^{12}\text{C}$  due to the electrolyte equilibration, CO is more enriched in  $^{12}\text{C}$  than  $\text{HCOO}^-$  (Fig. 2a). The difference in isotopic composition likely originates from the  $\text{CO}_2$ -to- $\text{HCOO}^-$  mechanism which, unlike  $\text{CO}_2$ -to-CO conversion, is known for not involving CO as an intermediate (e.g.,  $^*\text{CO}$ ).<sup>40-42</sup> Without an accumulation of intermediates involved in  $\text{HCOO}^-$  formation, its isotopic composition should closely track that of  $\text{CO}_{2(\text{aq})}$  available during OSRI. On the other hand, a buildup of CO population on a Cu surface is expected for CO formation.<sup>40,43,44</sup> In previous works, this buildup of CO has been suggested to result in a locally concentrated near-surface CO acting as an intermediate state for CO, and eventually, other higher-order product formation (e.g.,  $\text{C}_2\text{H}_4$ ).<sup>24,25,27</sup> This hypothesis has inspired improved  $\text{CO}_2$  reduction strategies by combining CO generating catalysts (e.g., Ag, Au) with Cu-based electrodes.<sup>45-48</sup> Furthermore, these studies infer that chemically adsorbed CO (i.e.,  $^*\text{CO}$ ) may not be the only configuration of CO as an intermediate. Therefore, we refer to all CO species during  $\text{CO}_2$

electroreduction, whether chemically bound or otherwise physically confined near the catalyst surface, as  $\text{CO}_{\text{int}}$ . The buildup and formation of a large reservoir of  $\text{CO}_{\text{int}}$  will lead to a lag between the available  $\text{CO}_{2(\text{aq})}$  (reagent) and CO (product) released at steady-state. Specifically, in an experiment that switches from one isotope of  $\text{CO}_{2(\text{aq})}$  ( $^{12}\text{C}$ ) to another ( $^{13}\text{C}$ ), CO produced is expected to be more enriched in  $^{12}\text{C}$  than the average isotopic composition of available  $\text{CO}_{2(\text{aq})}$  (Fig. 1a).

To understand this isotopic lag phenomenon quantitatively, we construct a mathematical model that describes a  $\text{CO}_{\text{int}}$  reservoir attached to a Cu surface during OSRI (Fig. 2b). The applicability of the model to the experimental observations was evaluated and confirmed based on its close reproduction of four key experimental results: ① the average isotopic fraction of  $\text{H}^{12}\text{COO}^-$ , ② the average isotopic fraction of  $^{12}\text{CO}$ , ③ the density of the  $\text{CO}_{\text{int}}$  reservoir per surface Cu atom ( $\text{Cu}_{\text{surf}}$ ), and ④ the isotopic fraction of  $^{12}\text{CO}_{\text{int}}$  at the  $\text{CO}_{\text{int}}$  reservoir by the end of OSRI (details available in Supplementary Text 6 and Figs. S13-14). Owing to the presence of the  $\text{CO}_{\text{int}}$  reservoir, the model reproduced the delayed exchange to  $^{13}\text{C}$  in the CO produced, leading to the trends shown in Figure 2b for the isotopic fraction of  $\text{H}^{12}\text{COO}^-$  and  $^{12}\text{CO}$  over time. Values ① and ② are essentially the areas of each curve for  $\text{H}^{12}\text{COO}^-$  and  $^{12}\text{CO}$  divided by the entire period (i.e., 120 min), respectively. Furthermore, the steady state ③ size of the  $\text{CO}_{\text{int}}$  reservoir predicted by the model can be compared to the experimental value measured after stopping the bias at the end of the second hour of OSRI. All CO present in the cell then is purged with Ar for one hour and collected in gas bag #2 (Fig. 1c). The amount of  $\text{CO}_{\text{int}}$  present at steady state near the Cu surface is determined after quantifying all the collected CO and subtracting the headspace and bulk electrolyte dissolved CO contributions (Methods and Fig. S15). The number of  $\text{Cu}_{\text{surf}}$  necessary to determine the  $\text{CO}_{\text{int}}$  density per  $\text{Cu}_{\text{surf}}$  atom can be derived from Pb underpotential deposition (Supplementary Text 7 and Fig. S16). Because of any possible structural changes that may take place as bias is applied, the electrochemically active surface area (ECSA) of the catalyst was determined post-electrolysis.<sup>39,49</sup> The model also predicts the trend of the isotopic fraction of  $^{12}\text{CO}_{\text{int}}$  throughout OSRI leading to value ④ at 120 min (Fig. S13d). The model-derived isotopic fraction of  $^{12}\text{CO}_{\text{int}}$  at this final time point can be compared to the experimental isotopic fraction, measured as 54%  $^{12}\text{CO}$ , for all CO remaining post-electrolysis and collected in gas bag #2 (Fig. 1c). Overall, the model closely reproduced the experimental values as summarized in Fig. 2c.

As stated earlier, the difference in isotopic composition between values ① and ② is a result of the  $\text{CO}_{\text{int}}$  reservoir being present during  $\text{CO}_2$  electrolysis. Changing experimental conditions to accelerate the rate of  $\text{CO}_{2(\text{aq})}$  exchange from  $^{12}\text{C}$  to  $^{13}\text{C}$  (e.g., by the use of a liquid flow cell simultaneously switching to a  $\text{KH}^{13}\text{CO}_3$  electrolyte) does not alter this difference (Fig. S17). The duration of operation upon substituting to  $^{13}\text{CO}_{2(\text{g})}$  is another parameter that could be considered, and a longer electrolysis period is not desirable as the larger amount of total products formed obscures the relative difference between  $\text{H}^{12}\text{COO}^-$  and  $^{12}\text{CO}$  (Fig. S18). Altogether, the chosen experimental conditions that define OSRI are adequate to assess the presence of the  $\text{CO}_{\text{int}}$  reservoir.

The results obtained from OSRI and reproduced by the model confirm the hypothesis of a  $\text{CO}_{\text{int}}$  reservoir present during  $\text{CO}_2$ RR. Furthermore, the size of the  $\text{CO}_{\text{int}}$  reservoir verified offers new insights into the local environment of catalytically active Cu surfaces during  $\text{CO}_2$  electrolysis. We find that the  $\text{CO}_{\text{int}}$  density is around 78  $\text{CO}_{\text{int}}$  per  $\text{Cu}_{\text{surf}}$ , which is much higher than monolayer coverage expected for  $^*\text{CO}$  alone (i.e., 1  $\text{CO}_{\text{int}}$  per  $\text{Cu}_{\text{surf}}$ ) (Fig. 2b). Assuming that this density of  $\text{CO}_{\text{int}}$  molecules is confined in a volume extending as far as  $\sim 100\ \mu\text{m}$  from the electrode (i.e., up to the Nernst diffusion layer), then its concentration is approximately 18 mM (where typical CO solubility in water is 1 mM). Such a high concentration (20 to 100 times the solubility) has previously been verified near the surface of gas evolving electrodes and is associated with gas bubble nucleation and growth.<sup>50-54</sup> Although not reported for CO specifically, its physical properties akin to  $\text{H}_2$  or  $\text{N}_2$  suggest it would behave similarly during electrolysis (Supplementary Text 8 and Table S7). Therefore, we expect the physical state of  $\text{CO}_{\text{int}}$  to approach a condensed gas phase on and near the electrode surface. Such a large accumulation of CO molecules is likely enabled by the physical properties of the electrode-gas-electrolyte interface formed during  $\text{CO}_2$  electrolysis. In presence of a large production of CO molecules, the Cu electrode can facilitate heterogeneous

bubble nucleation on its surface by lowering the energy barrier of this process.<sup>50-54</sup> We hypothesize that these favorable conditions for bubble formation enable the retention of a high CO<sub>int</sub> density close to the catalyst surface.

To understand the role of the CO<sub>int</sub> reservoir in the formation of C<sub>2+</sub> products, we investigated more negative potentials where CO<sub>2</sub>-to-C<sub>2+</sub> conversion takes place. Experimentally, not only were the C<sub>2+</sub> products also higher in <sup>12</sup>C content relative to HCOO<sup>-</sup>, but they shared a similar average isotopic composition with CO, highly suggesting that the CO<sub>int</sub> reservoir acts both as a source of product CO and as an intermediate pool for C<sub>2+</sub> (Fig. S19). The model was therefore expanded to reproduce the isotopic composition of C<sub>2+</sub> products, as well as HCOO<sup>-</sup> and CO, at more negative potentials. The conversion rate of the CO<sub>int</sub> reservoir was adjusted to include the amount of CO<sub>int</sub> consumed to C<sub>2+</sub> products (Supplementary Text 9). Once more, the model was found to closely reproduce the experimental data obtained during OSRI supporting the CO<sub>int</sub> reservoir as an intermediate to C<sub>2+</sub> formation. For instance, the isotopic composition of gas products measured in real time by GC-MS for the CO-derived products, such as CO and C<sub>2</sub>H<sub>4</sub>, matched closely with the trend expected by the model (Fig. 3a and Fig. S21). Similarly, the isotopic composition of HCOO<sup>-</sup> measured at different time intervals (e.g., 80 and 100 min) by <sup>1</sup>H NMR matched closely with the corresponding H<sup>12</sup>COO<sup>-</sup><sub>av</sub> expected by the model (Fig. S22). Furthermore, the model closely replicated all the experimental values ①-④ (Fig. S20). Overall, instead of the traditional reaction pathway of CO<sub>2</sub> to surface-bound \*CO and then to C<sub>2+</sub> products, we posit that CO<sub>2</sub> first reduces to CO<sub>int</sub> which accumulates to a concentrated reservoir near the catalyst surface before subsequent conversion to higher-order products (Fig. 3b).

Additionally, only a small fraction of the CO<sub>int</sub> reservoir is converted per second to produce CO, C<sub>2</sub>H<sub>4</sub>, EtOH, and n-PrOH (Fig. 3c). The relative portion of the CO<sub>int</sub> reservoir utilized per unit time (% s<sup>-1</sup>) does not increase significantly and reaches only up to 1.05% per second as the potential is biased more negative. Instead, the distribution of products formed from the CO<sub>int</sub> reservoir changes in favor of C<sub>2+</sub> (Fig. 3d). Simultaneously, this shift in selectivity coincides with an increase of the CO<sub>int</sub> density, roughly doubling from 78 to 147 molecules per Cu<sub>surf</sub> (Fig. 3d). These observations suggest that C<sub>2+</sub>-formation correlates with a sizeable amount of CO<sub>int</sub> per Cu<sub>surf</sub> (~100 CO<sub>int</sub>/Cu<sub>surf</sub>). Interestingly, we note that a CO<sub>int</sub> reservoir conversion of 1.05% per sec is equivalent to a conversion rate of ~1 CO<sub>int</sub> monolayer per sec. This indicates that, unlike a monolayer of CO<sub>int</sub>, a large CO<sub>int</sub> reservoir can sustain the necessary conditions to attain a conversion rate at the scale of a monolayer of intermediates per sec.

Previous works have commented on the importance of obtaining high CO surface coverage to facilitate C-C coupling.<sup>22,25,55</sup> The OSRI results suggest that this configuration extends to a CO<sub>int</sub> reservoir present near the catalyst surface which may act as the source for C<sub>2+</sub> formation downstream. Hence, the former notion of the traditional \*CO monolayer is replaced with a locally concentrated large population of CO molecules as intermediates. Furthermore, OSRI experimentally verifies the often-speculated idea of CO-rich environments on the surface of Cu catalysts during CO<sub>2</sub> electrolysis.<sup>24-27</sup>

To verify that the CO<sub>int</sub> reservoir is not unique to the Cu NP ensemble catalyst, the OSRI method was applied to an electropolished Cu foil, a well-known benchmark Cu catalyst for CO<sub>2</sub>RR. The potential range selected to study the Cu foil was negatively shifted in comparison to the Cu NP ensemble to generate a similar product distribution (Fig. S23 and Table S8). Cu foil exhibits a similar gap in <sup>12</sup>C isotopic fraction between HCOO<sup>-</sup> and all CO<sub>int</sub>-derived products (Fig. S24). Unlike the Cu NP ensemble, Cu foil displays a high FE towards CH<sub>4</sub> that allows for its isotopic distribution to be more thoroughly analyzed. The <sup>12</sup>C fraction of CH<sub>4</sub> is consistent with all other CO<sub>int</sub>-derived products which corroborates the importance of CO as an intermediate for CH<sub>4</sub> production during CO<sub>2</sub> electroreduction.<sup>15,56</sup> However, a collection of gases (i.e., CO, CH<sub>4</sub>, and C<sub>2</sub>H<sub>4</sub>) was detected when trying to identify the contents of the reservoir experimentally as described in Fig. 1c (Supplementary Text 10 and Fig. S25). The presence of products such as CH<sub>4</sub>, together with CO concentrated near the surface is expected to result from the morphological features of the Cu surface promoting retention of gases.<sup>57</sup> Therefore, the model was used to fit the Cu foil data while taking into consideration the presence of gases beyond CO as part of a larger reservoir regulating product formation and release (Supplementary Text 11 and Fig. S26). Ultimately, the model closely

replicates the experimental data thus confirming the existence of a CO<sub>int</sub> reservoir on Cu foil during CO<sub>2</sub>RR (Fig. S27).

Interestingly, both catalysts appear to enable C-C coupling after reaching a sufficiently high density of CO<sub>int</sub> per Cu<sub>surf</sub>. Similar to the Cu NP ensemble, analysis of the Cu foil indicates a transition from C<sub>1</sub> to C<sub>2+</sub> formation at a CO<sub>int</sub> density ~100 CO<sub>int</sub> per Cu<sub>surf</sub> (Fig. 4a). The Cu foil further resembles the Cu NP ensemble with a CO<sub>int</sub>-to-C<sub>2+</sub> conversion rate of ~1 CO<sub>int</sub> monolayer per sec which is achieved after reaching ~100 CO<sub>int</sub> per Cu<sub>surf</sub> (Fig. S28). These results suggest that a high surface coverage restricted to a monolayer does not provide the amount of CO<sub>int</sub> necessary for C<sub>2+</sub> formation. This principle is also in line with a recent finding showing that even a Ag catalyst can improve its otherwise negligible selectivity towards C<sub>2+</sub> products given a high enough CO pressure.<sup>58</sup> Taken these data, a key consideration in the development of catalysts moving forward should be increasing the CO<sub>int</sub> density at lower overpotentials. Accordingly, the Cu NP ensemble reaches an adequate CO<sub>int</sub> density at an overpotential 100 mV lower than the foil (Fig. 4b).

In addition to producing a sufficiently concentrated CO<sub>int</sub> reservoir, a catalyst's activity should also be determined by its innate ability to convert the CO<sub>int</sub> reservoir to C<sub>2+</sub>. So far, Cu-based electrocatalysts have been evaluated based on their C<sub>2+</sub> faradaic efficiency and turnover at a fixed potential. However, such analysis does not account for the availability of CO<sub>int</sub>, which is critical; without the sufficient formation of CO<sub>int</sub>, a catalyst is unlikely to form C<sub>2+</sub> efficiently. Therefore, considering both the applied potential and availability of CO<sub>int</sub> is necessary to accurately assess a catalyst's C-C coupling (i.e., the intrinsic C<sub>2+</sub> formation from C<sub>1</sub> intermediates) ability. This is readily apparent in the comparison of C<sub>2+</sub> turnover between the Cu NP ensemble and the foil around -0.85 V where the former displays a CO<sub>int</sub> reservoir three times as large as the latter (Fig. 4b). This difference in the size of the CO<sub>int</sub> reservoir brings into question whether the Cu foil may yield a C<sub>2+</sub> turnover comparable to the NP ensemble provided there is enough CO<sub>int</sub> allowed at a lower overpotential. However, we find this unlikely given the trend in the C<sub>2+</sub> TOF of the Cu foil (Fig. 4b). Despite reaching a CO<sub>int</sub> density of ~100 CO<sub>int</sub> per Cu<sub>surf</sub>, its TOF does not rise steeply to reach comparable levels as the NP ensemble; a TOF of 0.1 C<sub>2+</sub> per Cu<sub>surf</sub> s<sup>-1</sup> at -0.92 V is 4-fold lower than the NP ensemble whose TOF is 0.4 C<sub>2+</sub> per Cu<sub>surf</sub> s<sup>-1</sup> at only -0.86 V. Furthermore, under CO reduction (CORR) conditions with identical CO availability, we find the NP ensemble to exhibit higher TOF<sub>C2+</sub> than the Cu foil as well (Fig. S29). Hence, the formation of a concentrated CO<sub>int</sub> reservoir is necessary but not sufficient for high C<sub>2+</sub> turnover.

In addition, both catalysts reach noticeably higher levels of TOF<sub>C2+</sub> during CO<sub>2</sub>RR in comparison to CORR (Fig. S29). This likely results from the formation of the reservoir during the electroreduction of CO<sub>2</sub>, which sustains ~100 CO molecules per Cu<sub>surf</sub>. In contrast, within the 100 μm layer away from the catalyst surface, only 5 CO molecules per Cu<sub>surf</sub> would be available under CORR. The concentrated CO microenvironment formed during CO<sub>2</sub>RR overcomes the constraint of low CO solubility (1 mM in water at 1 atm, room temperature) which limits CORR activity in aqueous conditions. Therefore, instead of the concentration of CO<sub>2</sub>, the size of the CO<sub>int</sub> reservoir is a more accurate representation of the reactants necessary to the formation of multicarbons. We suggest that such considerations are also important for CO<sub>2</sub> reduction in gas-diffusion electrode (GDE) systems; recent works have reported the importance of optimizing both the CO<sub>2</sub> and CO availability to maximize C-C coupling.<sup>55,59,60</sup>

The results from the OSRI method suggest that both the contribution of CO<sub>int</sub> availability and intrinsic C-C coupling ability are necessary to a catalyst's CO<sub>2</sub>-to-C<sub>2+</sub> activity. Concretely, a good catalyst must possess the ability to form a large CO<sub>int</sub> reservoir at low overpotentials as well as exhibit high intrinsic activity for the coupling of CO<sub>int</sub>. The Cu foil's moderate C<sub>2+</sub> intrinsic activity is ascribed not only to its low intrinsic C-C coupling capacity but also to the high overpotential required to form a large enough CO<sub>int</sub> reservoir. Therefore, maximizing CO<sub>int</sub> availability at low overpotentials emerges as an additional parameter in future catalyst design, in addition to the necessary structural traits that favor C-C coupling.<sup>39,61,62</sup> Namely, CO<sub>int</sub> availability can be enhanced through improved retention of CO upon its formation. A few approaches along this line have been considered, such as modifying surface morphologies of electrodes to impact product release or functionalizing the catalyst with surface additives that promote gas affinity through increased



hydrophobicity.<sup>28,63-65</sup> Beyond catalyst design implications, these results indicate that further investigations to determine the intrinsic C-C coupling of Cu-based catalysts under controlled (micro)environments are needed.

In summary, we present OSRI, a unique method that probes the microenvironment surrounding Cu surfaces during CO<sub>2</sub>RR. It has led to the discovery of a concentrated reservoir of CO molecules near catalyst surfaces which is necessary for efficient C-C coupling. Instead of CO<sub>2</sub>, this reservoir is identified as a more accurate representation of the reactants determining the rate of multicarbon formation during CO<sub>2</sub>RR. Through these findings, the importance of the microenvironment formed during the reaction is better distinguished from the intrinsic activity of the catalyst surface. Furthermore, OSRI is a promising method to investigate the effects of the microenvironment in other catalytic reactions similar to CO<sub>2</sub>RR. Specifically, the significance of intermediates residing near the surface during multi-step electrocatalytic reactions can be gauged, thus guiding future improvements in catalysts' selectivity and activity.

## Materials and Methods

### *Nanoparticle synthesis and electrode fabrication*

7 nm copper nanoparticles (NPs) were synthesized as previously reported.<sup>39</sup> Nanoparticle concentrations by mass of copper were measured by inductively-coupled plasma optical emission spectroscopy (Perkin Elmer Optima 7000 DV), after which 68.9 µg of copper was deposited on 1 cm<sup>2</sup> area of carbon paper (Sigracet 29AA, Fuel Cell Store) to make working electrodes. Cu foil (0.1mm thick, Puratronic, 99.999%) was electropolished before utilization in 85% phosphoric acid at 3V against a counter electrode for 1 min. Once treated, the Cu foil was thoroughly rinsed with deionized water and dried with N<sub>2</sub> gas. The electrode of 4 cm<sup>2</sup> geometric surface area was placed inside an electrochemical cell for further testing.

### *On-stream Substitution of Reactant Isotopes*

All electrochemical measurements were carried in a custom-made H-cell consisting of two main compartments separated by a Selemion AMV anion exchange membrane (AEM). Ag/AgCl (WPI, 3M KCl) was used as a reference electrode and a platinum wire was used as a counter electrode. 0.1 M KHCO<sub>3</sub> electrolyte was prepared by purging a 0.05 M K<sub>2</sub>CO<sub>3</sub> (99.997% trace metal basis) solution with CO<sub>2(g)</sub> overnight. Both the working and counter chamber were filled with 15 mL of the electrolyte and vigorous stirring was maintained in the working chamber. The input stream of CO<sub>2(g)</sub> was humidified by being bubbled through DI water before being introduced into the cell. Before each measurement, the 15 mL catholyte was purged with 20 sccm <sup>12</sup>CO<sub>2(g)</sub> for 15 - 20 min until saturated. Then, <sup>12</sup>CO<sub>2(g)</sub> was purged while applying a cathodic bias for 60 min and subsequently switched to <sup>13</sup>CO<sub>2(g)</sub> (<sup>13</sup>C dioxide, 99 atom % <sup>13</sup>C, 99.93 atom % <sup>16</sup>O) while maintaining the same potential for another 60 min. Depending on the operating conditions, the flow rate was adjusted to 20, 10, or 5 sccm. For instance, low flow rates were used for conditions that exhibit low current densities (e.g., at more positive potentials). This ensured higher concentrations of gas products to be measured in real-time using the gas chromatograph. All electrode potentials measured against 3M KCl Ag/AgCl reference were converted to the RHE scale using  $E \text{ (vs RHE)} = E \text{ (vs Ag/AgCl)} + 0.210 \text{ V} + 0.0591 \times \text{pH}$ . For all electrochemical experiments, 84% of ohmic loss was compensated by the potentiostat (Biologic) in real-time and the remaining 16% was manually post-corrected.

The concentration of gases produced throughout OSRI were measured regardless of their isotopic identity using a gas chromatograph (SRI GC) connected at the outlet of the cell. Gas chromatograph is equipped with a molecular sieve 13X (1/8" × 6') and hayesep D (1/8" × 6') column with Ar flowing as a carrier gas. Sample for gas chromatography was collected at 20 minute intervals and the separated gas products were analyzed by a thermal conductivity detector (for H<sub>2</sub>) and a flame ionization detector (for CO and hydrocarbons). Quantification of the products was performed with conversion factors derived from the standard calibration gases and the concentration of gas measured was further converted to partial current density.

Upon substitution of the reactant isotope from  $^{12}\text{CO}_{2(\text{g})}$  to  $^{13}\text{CO}_{2(\text{g})}$ , all produced gases were collected to determine their isotopic composition. 2L Supel-Inert Multi-Layer Foil gas bag (gas bag #1) was connected to the exhaust of the SRI GC sampling loop at the same time as the onstream substitution at 60 min. After another 60 min of electrolysis while purging  $^{13}\text{CO}_{2(\text{g})}$ , application of bias was terminated, and the gas stream was substituted with Ar. Gas bag #1 was simultaneously sealed and substituted for a second bag (gas bag #2) to collect any leftover gases still present inside the cell to determine the size and composition of the  $\text{CO}_{\text{int}}$  reservoir (see Methods section “Determining the size and isotopic composition of the  $\text{CO}_{\text{int}}$  reservoir”).

The isotopic composition of gas products in gas bag #1 was determined by GC-MS using an AutoSpec Premier mass spectrometer (Waters, Manchester, UK), equipped with an Agilent 7890A gas chromatograph, and an electron impact ion source. The collected gases were sampled and manually injected using a gas-tight 1 mL syringe (Agilent PN 5190-1531). They were pushed through a Supelco, Carboxen- 1010 PLOT column with He as a carrier gas to separate CO,  $\text{CH}_4$ , and  $\text{C}_2\text{H}_4$  from  $\text{N}_2$ ,  $\text{O}_2$  and  $\text{CO}_2$  (Fig. S1). The mass spectrograms were analyzed to extract the isotopic composition of all  $\text{CO}_2\text{RR}$  gas products as described in Supplementary Text 1.

Meanwhile, the liquid products accumulated during OSRI were analyzed by qNMR (Bruker AV-600) using dimethyl sulfoxide as an internal standard. Solvent presaturation technique was implemented to suppress the water peak. The collection of all liquid products was ensured by analyzing the catholyte and the AEM. The latter was soaked in 15 mL blank electrolyte overnight to ensure all trapped products would diffuse back into the liquid (Supplementary Text 2). Further isotope analysis was carried on the liquid products combining  $^1\text{H}$  with  $^{13}\text{C}$  NMR on the same instrument.  $^{13}\text{C}$  NMR required long acquisition time (>9h) to accumulate enough signal due to low concentrations. The isotopic composition of liquid products (e.g.,  $\text{HCOO}^-$ , EtOH) was determined by decoupling the signals from their multiple isotopologues as described in Supplementary Text 3. Faradaic efficiencies (FE) were calculated from the amount of charge passed to produce each product divided by the total charge passed at a specific time (gas) or during the overall run (liquid).

#### *Determining the size and isotopic composition of the $\text{CO}_{\text{int}}$ reservoir*

After the second hour of electrolysis while purging  $^{13}\text{CO}_{2(\text{g})}$ , the bias was terminated and all CO present in the cell was purged out with Ar for 60 min and collected in gas bag #2. Ar purge of 60 min ensured that there were no remaining gases in the working electrode chamber. Depending on the flow rate employed for each experiment, ranging from 5 to 20 sccm, gas bag #2 was filled with a total gas volume of 300 to 1200 mL, respectively. The low CO concentration collected in gas bag #2 was measured after injecting the bag content into another gas chromatograph (Agilent 7890B GC) setup for manual injection. This gas chromatograph is equipped with a molecular sieve SA (60/80" x 6'), hayesep Q (80/100" x 6'), and hayesep Q (80/100" x 1.5') column with Ar flowing as a carrier gas. The same detectors (i.e., FID and TCD) listed for the SRI GC are used. Using the measured CO concentration, the total amount of CO molecules was calculated considering the total volume of gas collected. Gas bag #2 contained CO collected from the headspace, dissolved in the bulk electrolyte, and locally concentrated near the catalyst surface (i.e.,  $\text{CO}_{\text{int}}$  reservoir), all present upon stopping bias. CO present in the cell headspace was determined from the concentration of CO measured at steady state during electrolysis (SRI GC) and the headspace volume of 30 mL. Furthermore, Henry's law was applied to obtain the number of dissolved CO in equilibrium with that headspace. The size of the  $\text{CO}_{\text{int}}$  reservoir was estimated by subtracting both values from the total amount of CO collected in gas bag #2. The isotopic composition of the  $\text{CO}_{\text{int}}$  reservoir was determined following the GC-MS procedure (described for gas bag #1) applied to gas bag #2. The composition of the  $\text{CO}_{\text{int}}$  reservoir is assumed to be identical to the headspace and dissolved CO. The same method of quantification was employed at more negative potentials.

#### *Electrochemically active surface area and Cu surface atoms determination*

Lead underpotential deposition was conducted immediately post-electrolysis in a solution of 0.1 M  $\text{NaClO}_4$ , 10 mM  $\text{HClO}_4$ , and 3 mM  $\text{Pb(II)(ClO}_4)_2$ . Cyclic voltammetry in the Pb underpotential region was conducted at 10 mV/s six times, for which the cycles were confirmed

consistent, and the fifth scan was reported. The potentials are referenced against a 1.0 M KCl Ag/AgCl electrode.

The number of Cu surface atoms was then determined using the assumption that each of the low index facets (100), (110), and (111) are equally likely to be present on the surface. We used the relationship between the number of Cu atoms and surface area for each facet as established in the work of Giri and Sakar to determine the number of surface Cu atoms from the measured Cu surface area by Pb UPD.<sup>66</sup>

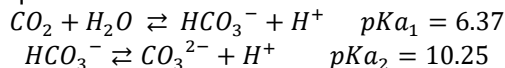
$$\begin{aligned} \text{Planar density of Cu (100) plane} &= 15.3065 \times 10^{14} \frac{\text{atoms}}{\text{cm}^2} \\ \text{Planar density of Cu (110) plane} &= 10.8371 \times 10^{14} \frac{\text{atoms}}{\text{cm}^2} \\ \text{Planar density of Cu (111) plane} &= 17.7556 \times 10^{14} \frac{\text{atoms}}{\text{cm}^2} \end{aligned}$$

#### COMSOL® Multiphysics simulation

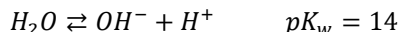
The change in isotopic composition taking place during the purge of <sup>13</sup>CO<sub>2</sub> gas into a <sup>12</sup>CO<sub>2</sub> equilibrated electrolyte was simulated using COMSOL® Multiphysics. The transport of species present was calculated for the bulk volume of the well-mixed electrolyte. “Bubbly Flow, Laminar Flow” module was used to solve for the velocity and mass transfer of CO<sub>2</sub> bubbles into the liquid electrolyte. Assuming only a small volume fraction is occupied by the bubbles, the Navier-Stokes equations were used only to solve for the flow of the liquid phase while the velocity of the bubbles was determined by a slip model. The gas mass flux was set to replicate the experimental flow rate employed during OSRI (e.g., 5 sccm) with a bubble size of 0.4 cm. The number of bubbles per unit volume is tracked over time within the electrolyte to calculate the total interfacial area *a* (m<sup>2</sup>). Mass transport *m<sub>gl</sub>* (kg.s<sup>-1</sup>) taking place at this interface was calculated using two-film theory:

$$m_{gl} = k(c^* - c)Ma, \quad c^* = \frac{p + p_{ref}}{H}$$

where *k* (m.s<sup>-1</sup>) corresponds to the mass transfer coefficient, *c* (mol.m<sup>-3</sup>) the concentration of the gas dissolved in solution, *M* (kg.mol<sup>-1</sup>) the gas molecular weight, *p* (Pa) the gas pressure, and *H* is Henry’s constant (Pa.m<sup>3</sup>.mol<sup>-1</sup>). Upon dissolution, the further equilibration of CO<sub>2</sub> at pH < 7 is described by the following equations:



Water self-ionization equilibrium is also included:



Using their respective equilibrium constants, the concentrations of all species present in the electrolyte were solved for, using the “Transport of Dilute Species” module. Dissolved CO<sub>2(aq)</sub>, bicarbonate anions (HCO<sub>3</sub><sup>-</sup>), carbonate anions (CO<sub>3</sub><sup>2-</sup>), hydroxide anions (OH<sup>-</sup>), protons (H<sup>+</sup>), and potassium cations (K<sup>+</sup>) were all accounted for during the time dependent study. All <sup>12</sup>C and <sup>13</sup>C equivalents were considered for all carbon containing species. The initial concentration of all species was established assuming the 0.1 M KH<sup>12</sup>CO<sub>3</sub> electrolyte is equilibrated under <sup>12</sup>CO<sub>2</sub> saturated atmosphere and respects the condition of electroneutrality:

$$\sum_i z_i c_i = 0$$

Following the introduction of <sup>13</sup>CO<sub>2(g)</sub>, the transport of all solvated species was set to respect mass conservation such as:

$$\frac{\partial c_i}{\partial t} + \nabla \cdot \mathbf{J} + \mathbf{u} \cdot \mathbf{c}_i = R_i, \quad \mathbf{J}_i = -D_i \nabla c_i - z_i u_{m,i} F c_i \nabla V$$

where *c<sub>i</sub>* the concentration of the species, *D<sub>i</sub>* their diffusion coefficient, *R<sub>i</sub>* their reaction rate expression, *u* the mass average velocity vector, *J<sub>i</sub>* the mass flux diffusive flux vector, *z<sub>i</sub>* the charge number of the ionic species, *u<sub>m,i</sub>* their ionic mobility, *F* is Faraday’s constant, and *V* the electric potential. The velocity *u* describes the convective transport that results from the magnetic stirring in the cell as well as the bubbly flow solved in the previous module. All constants utilized for the simulation are summarized in Table S6.

### OSRI kinetic model

Molecular mass flow taking place during OSRI was modeled to reproduce the composition of isotopes observed in the products. The model was built based on the kinetic relationship between supplied  $\text{CO}_2(\text{g})$ , available  $\text{CO}_2(\text{aq})$ , a  $\text{CO}_{\text{int}}$  reservoir, and all  $\text{CO}_2\text{RR}$  products. Once determined mathematically as described in the Supplementary Text 6, the model was run using MATLAB.

### CO reduction measurements

CO reduction experiments were conducted in a similar 3-electrode electrochemical H-cell constructed from PTFE, using 0.1 M KOH (Sigma, 99.99%) as electrolyte. CO (99.99%, Praxair) was purged through the electrolyte for at least 30 minutes before electrolysis and maintained at 15 sccm throughout electrolysis. Hg/HgO 1 M NaOH (0.13 V vs. SHE) reference electrode and Neosepta AHA membrane were used for their tolerance to the alkaline electrolyte. Electrolysis was conducted for 30 minutes to an hour before gas and liquid samples were collected. All gas and liquid products were analyzed using the same procedure described above for GC and NMR measurements, respectively.

### Acknowledgments

This work was supported by the Director, Office of Science, Office of Basic Energy Sciences, Chemical Sciences, Geosciences, & Biosciences Division, of the US Department of Energy under Contract DE-AC02-05CH11231, FWP CH030201 (Catalysis Research Program). ICP-OES was supported by the Microanalytical Facility, College of Chemistry, UC Berkeley. We thank College of Chemistry's NMR facility for resources provided and the staff for their assistance. Instruments in the CoC-NMR are supported in part by NIH S10OD024998. We thank Z. Zhou at the QB3 Chemistry Mass Spectrometry Facility for her assistance with GC-MS measurements. Computational work using COMSOL® Multiphysics was done at the Molecular Graphics and Computation Facility, UC Berkeley, which is supported by NIH S10OD023532. D.K. and S.Y. acknowledge support from the Samsung Scholarship.

### References

1. De Luna, P. *et al.* What would it take for renewably powered electrosynthesis to displace petrochemical processes? *Science* 364 (2019).
2. Blanco, D. E. & Modestino, M. A. Organic electrosynthesis for sustainable chemical manufacturing. *Trends Chem.* 1, 8-10 (2019).
3. Na, J. *et al.* General technoeconomic analysis for electrochemical coproduction coupling carbon dioxide reduction with organic oxidation. *Nat. Comm.* 10, 1-13 (2019).
4. Kim, D. *et al.* Selective  $\text{CO}_2$  electrocatalysis at the pseudocapacitive nanoparticle/ordered-ligand interlayer. *Nat. Energy*, 1-11 (2020).
5. Ramaswamy, N. *et al.* Hydrogen oxidation reaction in alkaline media: Relationship between electrocatalysis and electrochemical double-layer structure. *Nano Energy* 41, 765-771 (2017).
6. Chen, W. *et al.* Probing complex electrocatalytic reactions using electrochemical infrared spectroscopy. *Curr. Opin. Electrochem.* 14, 113-123 (2019).
7. Zaera, F. Probing liquid/solid interfaces at the molecular level. *Chem. Rev.* 112, 2920-2986 (2012).
8. Zhu, Y., Wang, J., Chu, H., Chu, Y.-C. & Chen, H. M. In Situ/Operando Studies for Designing Next-Generation Electrocatalysts. *ACS Energy Lett.* 5, 1281-1291 (2020).
9. Lancaster, L., Abdallah, W., Banta, S. & Wheeldon, I. Engineering enzyme microenvironments for enhanced biocatalysis. *Chem. Soc. Rev.* 47, 5177-5186 (2018).

10. Colquhoun, H. M., Stoddart, J. F. & Williams, D. J. Second-Sphere Coordination—a Novel Rôle for Molecular Receptors. *Angew. Chem. Int. Ed. in English* 25, 487-507 (1986).
11. Hale, L. V. & Szymczak, N. K. Hydrogen transfer catalysis beyond the primary coordination sphere. *ACS Catal.* 8, 6446-6461 (2018).
12. Cao, Y., Li, X. & Ge, J. Enzyme Catalyst Engineering toward the Integration of Biocatalysis and Chemocatalysis. *Trends Biotechnol.* (2021).
13. Vázquez-González, M., Wang, C. & Willner, I. Biocatalytic cascades operating on macromolecular scaffolds and in confined environments. *Nat. Catal.* 3, 256-273 (2020).
14. Zhang, Y., Wang, Q. & Hess, H. Increasing enzyme cascade throughput by pH-engineering the microenvironment of individual enzymes. *ACS Catal.* 7, 2047-2051 (2017).
15. Nitopi, S. *et al.* Progress and perspectives of electrochemical CO<sub>2</sub> reduction on copper in aqueous electrolyte. *Chem. Rev.* 119, 7610-7672 (2019).
16. Kim, Y. *et al.* Time-resolved observation of C–C coupling intermediates on Cu electrodes for selective electrochemical CO<sub>2</sub> reduction. *Energy Environ. Sci.* 13, 4301-4311 (2020).
17. Pérez-Gallent, E., Figueiredo, M. C., Calle-Vallejo, F. & Koper, M. T. Spectroscopic observation of a hydrogenated CO dimer intermediate during CO reduction on Cu (100) electrodes. *Angew. Chem.* 129, 3675-3678 (2017).
18. Wuttig, A., Ryu, J. & Surendranath, Y. Electrolyte competition controls surface binding of CO intermediates to CO<sub>2</sub> reduction catalysts. *Preprint at <https://doi.org/10.26434/chemrxiv-2019-7929038>*, v2 (2019).
19. Li, F. *et al.* Molecular tuning of CO<sub>2</sub>-to-ethylene conversion. *Nature* 577, 509-513 (2020).
20. Chou, T.-C. *et al.* Controlling the oxidation state of the Cu electrode and reaction intermediates for electrochemical CO<sub>2</sub> reduction to ethylene. *J. Am. Chem. Soc.* 142, 2857-2867 (2020).
21. Gunathunge, C. M., Ovalle, V. J., Li, Y., Janik, M. J. & Waegele, M. M. Existence of an electrochemically inert CO population on Cu electrodes in alkaline pH. *ACS Catal.* 8, 7507-7516 (2018).
22. Huang, Y., Handoko, A. D., Hirunsit, P. & Yeo, B. S. Electrochemical reduction of CO<sub>2</sub> using copper single-crystal surfaces: effects of CO\* coverage on the selective formation of ethylene. *ACS Catal.* 7, 1749-1756 (2017).
23. Sandberg, R. B., Montoya, J. H., Chan, K. & Nørskov, J. K. CO-CO coupling on Cu facets: Coverage, strain and field effects. *Surf. Sci.* 654, 56-62 (2016).
24. Wuttig, A. *et al.* Tracking a common surface-bound intermediate during CO<sub>2</sub>-to-fuels catalysis. *ACS Cent. Sci.* 2, 522-528 (2016).
25. Clark, E. L. & Bell, A. T. Direct observation of the local reaction environment during the electrochemical reduction of CO<sub>2</sub>. *J. Am. Chem. Soc.* 140, 7012-7020 (2018).
26. Jiang, S., Klingan, K., Pasquini, C. & Dau, H. New aspects of operando Raman spectroscopy applied to electrochemical CO<sub>2</sub> reduction on Cu foams. *J. Chem. Phys.* 150, 041718 (2019).
27. Klingan, K. *et al.* Reactivity determinants in electrodeposited Cu foams for electrochemical CO<sub>2</sub> reduction. *ChemSusChem* 11, 3449-3459 (2018).
28. Wakerley, D. *et al.* Bio-inspired hydrophobicity promotes CO<sub>2</sub> reduction on a Cu surface. *Nat. Mater.* 18, 1222-1227 (2019).
29. Baturina, O. *et al.* Effect of nanostructured carbon support on copper electrocatalytic activity toward CO<sub>2</sub> electroreduction to hydrocarbon fuels. *Catal. Today* 288, 2-10 (2017).
30. O'Mara, P. B. *et al.* Cascade reactions in nanozymes: Spatially separated active sites inside Ag-Core–Porous-Cu-shell nanoparticles for multistep carbon dioxide reduction to higher organic molecules. *J. Am. Chem. Soc.* 141, 14093-14097 (2019).
31. Dunwell, M. *et al.* Examination of near-electrode concentration gradients and kinetic impacts on the electrochemical reduction of CO<sub>2</sub> using surface-enhanced infrared spectroscopy. *ACS Catal.* 8, 3999-4008 (2018).
32. Heyes, J., Dunwell, M. & Xu, B. CO<sub>2</sub> reduction on Cu at low overpotentials with surface-enhanced in situ spectroscopy. *J. Phys. Chem. C* 120, 17334-17341 (2016).

33. Heidary, N., Ly, K. H. & Kornienko, N. Probing CO<sub>2</sub> conversion chemistry on nanostructured surfaces with Operando vibrational spectroscopy. *Nano Lett.* 19, 4817-4826 (2019).
34. Handoko, A. D., Wei, F., Yeo, B. S. & Seh, Z. W. Understanding heterogeneous electrocatalytic carbon dioxide reduction through operando techniques. *Nat. Catal.* 1, 922-934 (2018).
35. Osawa, M., Ataka, K.-I., Yoshii, K. & Nishikawa, Y. Surface-enhanced infrared spectroscopy: the origin of the absorption enhancement and band selection rule in the infrared spectra of molecules adsorbed on fine metal particles. *Appl. Spectrosc.* 47, 1497-1502 (1993).
36. Schatz, G. C. Theoretical studies of surface enhanced Raman scattering. *Acc. Chem. Res.* 17, 370-376 (1984).
37. Stiles, P. L., Dieringer, J. A., Shah, N. C. & Van Duyne, R. P. Surface-enhanced Raman spectroscopy. *Annu. Rev. Anal. Chem.* 1, 601-626 (2008).
38. Kas, R. *et al.* In-situ infrared spectroscopy applied to the study of the electrocatalytic reduction of CO<sub>2</sub>: Theory, practice and challenges. *ChemPhysChem* (2019).
39. Li, Y. *et al.* Electrochemically scrambled nanocrystals are catalytically active for CO<sub>2</sub>-to-multicarbon. *Proc. Natl. Acad. Sci. USA* 117, 9194-9201 (2020).
40. Peterson, A. A., Abild-Pedersen, F., Studt, F., Rossmeisl, J. & Nørskov, J. K. How copper catalyzes the electroreduction of carbon dioxide into hydrocarbon fuels. *Energy Environ. Sci.* 3, 1311-1315 (2010).
41. Hori, Y. i. in *Modern aspects of electrochemistry* 89-189 (Springer, 2008).
42. Chernyshova, I. V., Somasundaran, P. & Ponnurangam, S. On the origin of the elusive first intermediate of CO<sub>2</sub> electroreduction. *Proc. Natl. Acad. Sci.* 115, E9261-E9270 (2018).
43. Hansen, H. A., Varley, J. B., Peterson, A. A. & Nørskov, J. K. Understanding Trends in the Electrocatalytic Activity of Metals and Enzymes for CO<sub>2</sub> Reduction to CO. *J. Phys. Chem. Lett.* 4, 388-392 (2013).
44. Gattrell, M., Gupta, N. & Co, A. A review of the aqueous electrochemical reduction of CO<sub>2</sub> to hydrocarbons at copper. *J. Electroanal. Chem.* 594, 1-19 (2006).
45. Gurudayal *et al.* Sequential cascade electrocatalytic conversion of carbon dioxide to C–C coupled products. *ACS Appl. Energy Mater.* 2, 4551-4559 (2019).
46. Lum, Y. & Ager, J. W. Sequential catalysis controls selectivity in electrochemical CO<sub>2</sub> reduction on Cu. *Energy Environ. Sci.* 11, 2935-2944 (2018).
47. Gao, J. *et al.* Selective C–C Coupling in Carbon Dioxide Electroreduction via Efficient Spillover of Intermediates As Supported by Operando Raman Spectroscopy. *J. Am. Chem. Soc.* 141, 18704-18714 (2019).
48. Morales-Guio, C. G. *et al.* Improved CO<sub>2</sub> reduction activity towards C<sub>2+</sub> alcohols on a tandem gold on copper electrocatalyst. *Nat. Catal.* 1, 764-771 (2018).
49. Phan, T. H. *et al.* Emergence of Potential-Controlled Cu-Nanocuboids and Graphene-Covered Cu-Nanocuboids under Operando CO<sub>2</sub> Electroreduction. *Nano Lett.* 21, 2059-2065 (2021).
50. Vogt, H. On the supersaturation of gas in the concentration boundary layer of gas evolving electrodes. *Electrochim. Acta* 25, 527-531 (1980).
51. German, S. R. *et al.* Electrochemistry of single nanobubbles. Estimating the critical size of bubble-forming nuclei for gas-evolving electrode reactions. *Faraday Discuss.* 193, 223-240 (2016).
52. Chen, Q., Wiedenroth, H. S., German, S. R. & White, H. S. Electrochemical nucleation of stable N<sub>2</sub> nanobubbles at Pt nanoelectrodes. *J. Am. Chem. Soc.* 137, 12064-12069 (2015).
53. Ren, H., German, S. R., Edwards, M. A., Chen, Q. & White, H. S. Electrochemical generation of individual O<sub>2</sub> nanobubbles via H<sub>2</sub>O<sub>2</sub> oxidation. *J. Phys. Chem. Lett.* 8, 2450-2454 (2017).
54. Zhao, X., Ren, H., & Luo, L. Gas bubbles in electrochemical gas evolution reactions, *Langmuir.* 35, 5392-5408 (2019).

55. Tan, Y. C., Lee, K. B., Song, H. & Oh, J. Modulating local CO<sub>2</sub> concentration as a general strategy for enhancing C–C coupling in CO<sub>2</sub> electroreduction. *Joule* 4, 1104-1120 (2020).
56. Zhou, X. *et al.* Stabilizing Cu<sup>2+</sup> Ions by Solid Solutions to Promote CO<sub>2</sub> Electroreduction to Methane. *J. Am. Chem. Soc.* 144, 2079-2084, doi:10.1021/jacs.1c12212 (2022).
57. Xu, W., Lu, Z., Sun, X., Jiang, L. & Duan, X. Superwetting electrodes for gas-involving electrocatalysis. *Acc. Chem. Res.* 51, 1590-1598 (2018).
58. Raaijman, S. J., Schellekens, M. P., Corbett, P. J. & Koper, M. T. High-Pressure CO Electroreduction at Silver Produces Ethanol and Propanol. *Angew. Chem. Int. Ed.* 60, 21732-21736 (2021).
59. Wang, X. *et al.* Mechanistic reaction pathways of enhanced ethylene yields during electroreduction of CO<sub>2</sub>–CO co-feeds on Cu and Cu-tandem electrocatalysts. *Nat. Nanotechnol.* 14, 1063-1070 (2019).
60. Xing, Z., Hu, L., Ripatti, D. S., Hu, X. & Feng, X. Enhancing carbon dioxide gas-diffusion electrolysis by creating a hydrophobic catalyst microenvironment. *Nat. Comm.* 12, 1-11 (2021).
61. Jung, H. *et al.* Electrochemical fragmentation of Cu<sub>2</sub>O nanoparticles enhancing selective C–C coupling from CO<sub>2</sub> reduction reaction. *J. Am. Chem. Soc.* 141, 4624-4633 (2019).
62. Loiudice, A. *et al.* Tailoring copper nanocrystals towards C<sub>2</sub> products in electrochemical CO<sub>2</sub> reduction. *Angew. Chem. Int. Ed.* 55, 5789-5792 (2016).
63. Burdyny, T. *et al.* Nanomorphology-enhanced gas-evolution intensifies CO<sub>2</sub> reduction electrochemistry. *ACS Sustain. Chem. Eng.* 5, 4031-4040 (2017).
64. Khan, S., Hwang, J., Horn, Y.-S. & Varanasi, K. K. Catalyst-proximal plastrons enhance activity and selectivity of carbon dioxide electroreduction. *Cell Rep. Phys. Sci.* 2, 100318 (2021).
65. Yue, P. *et al.* Triple-phase electrocatalysis for the enhanced CO<sub>2</sub> reduction to HCOOH on a hydrophobic surface. *Chem. Eng. J.* 405, 126975 (2021).
66. Giri, S.D. & Sarkar, A. Estimating surface area of copper powder: A comparison between electrochemical, microscopy and laser diffraction methods. *Adv. Powder Technol.* 29, 3520-3526 (2018).

## Figures

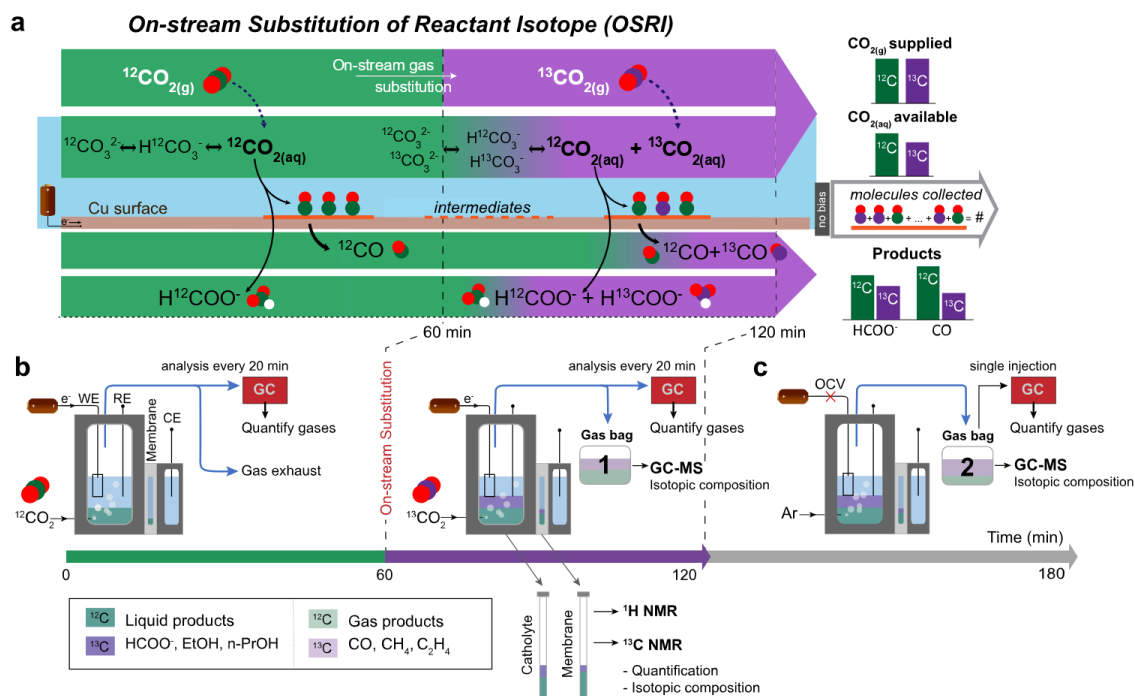


**Figure 1. Study of Cu for  $\text{CO}_2$  electroreduction by OSRI.** **a**, Schematic describing OSRI and the catalytic results of Cu. Cathodic bias is applied and maintained for 2 hours while the 0.1 M  $\text{KH}^{12}\text{CO}_3$  electrolyte is purged with  $^{12}\text{CO}_2(\text{g})$  (green) for the first hour followed by  $^{13}\text{CO}_2(\text{g})$  (purple) during the second hour. **b**, The experimental setup of OSRI. Products that contain  $^{12}\text{C}$  (green) and  $^{13}\text{C}$  (purple) accumulate in the gas (gas bag #1) and liquid phase (electrolyte) for isotopic analysis by GC-MS and NMR, respectively. All effluent gases are collected in gas bag #1 for the second hour only. Regular quantification of gas products is conducted by sampling the outlet stream at 20 minute intervals by GC. NMR spectroscopy is used to quantify and determine the isotopic composition of the liquid products accumulated after 2 hours in both the catholyte and the anionic membrane. Formate is the only product that accumulates in the membrane during OSRI. **c**, After 2 hours of electrolysis, the application of bias is terminated, and the electrolyte is purged with Ar into a second gas bag (gas bag #2) for another hour to collect all the gases remaining in the chamber. The contents of gas bag #2 are analyzed using GC (quantification) and GC-MS (isotopic composition).



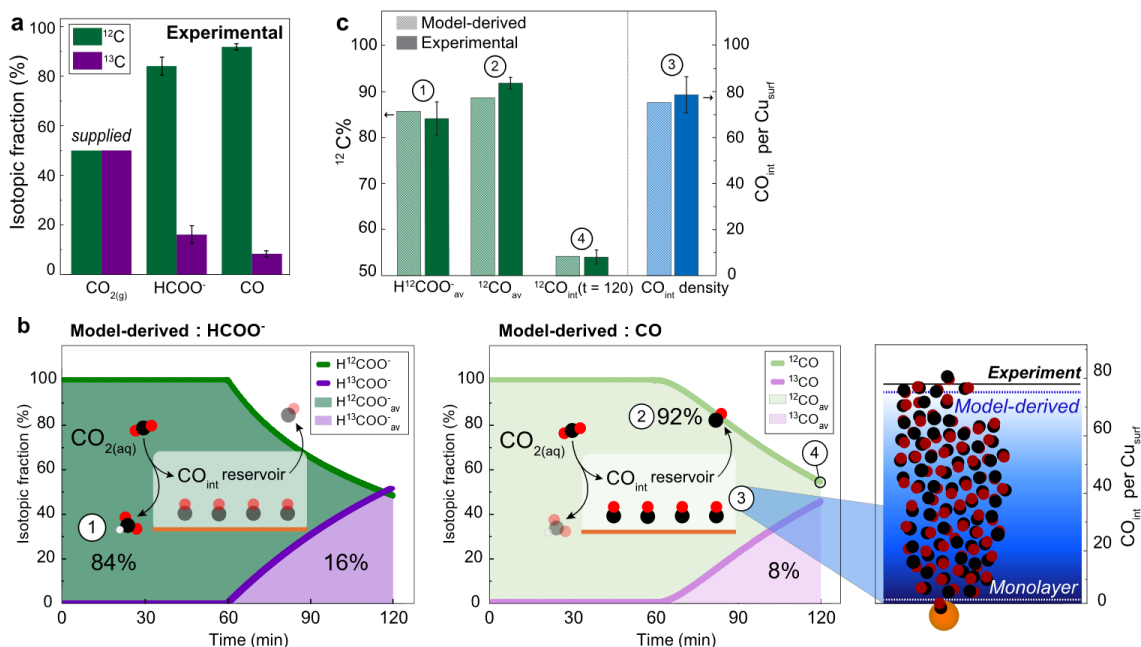


**Figure 2. Identification of the  $\text{CO}_{\text{int}}$  reservoir on the Cu NP ensemble.** **a**, Isotopic composition of  $\text{CO}_{2(g)}$  supplied and the products of  $\text{CO}_2\text{RR}$  measured during OSRI at  $-0.6$  V vs RHE. **b**, Model-derived isotopic composition of  $\text{HCOO}^-$  and  $\text{CO}$  produced overtime during OSRI considering the presence of a  $\text{CO}_{\text{int}}$  reservoir of constant size at steady state. The green areas under the  $\text{H}^{12}\text{COO}^-$  (dark green) and  $^{12}\text{CO}$  (light green) curves divided by the total period (2 hrs) respectively indicate the average isotopic fraction of ①  $^{12}\text{HCOO}^-$  and ②  $^{12}\text{CO}$  for the entire run. ④  $^{12}\text{CO}_{\text{int}}$  at the end of OSRI correspond to  $^{12}\text{CO}_{\text{int}}(t = 120 \text{ min})$ . The ③ steady state density of  $\text{CO}_{\text{int}}$  per  $\text{Cu}_{\text{surf}}$  measured experimentally and reproduced by the model are illustrated and compared to the monolayer of adsorbed  $^*\text{CO}$ . The number of  $\text{Cu}_{\text{surf}}$  was estimated by measuring the post-electrolysis electrochemically active surface area by Pb underpotential deposition. **c**, Comparison of model-derived and experimental values for the average isotopic fraction of ①  $\text{H}^{12}\text{COO}^-$  and ②  $^{12}\text{CO}$  during OSRI, ③ the steady state  $\text{CO}_{\text{int}}$  density, and ④ the isotopic fraction  $^{12}\text{CO}_{\text{int}}(t = 120 \text{ min})$ . Error bars are one standard deviation of three independent measurements for the experimental data.

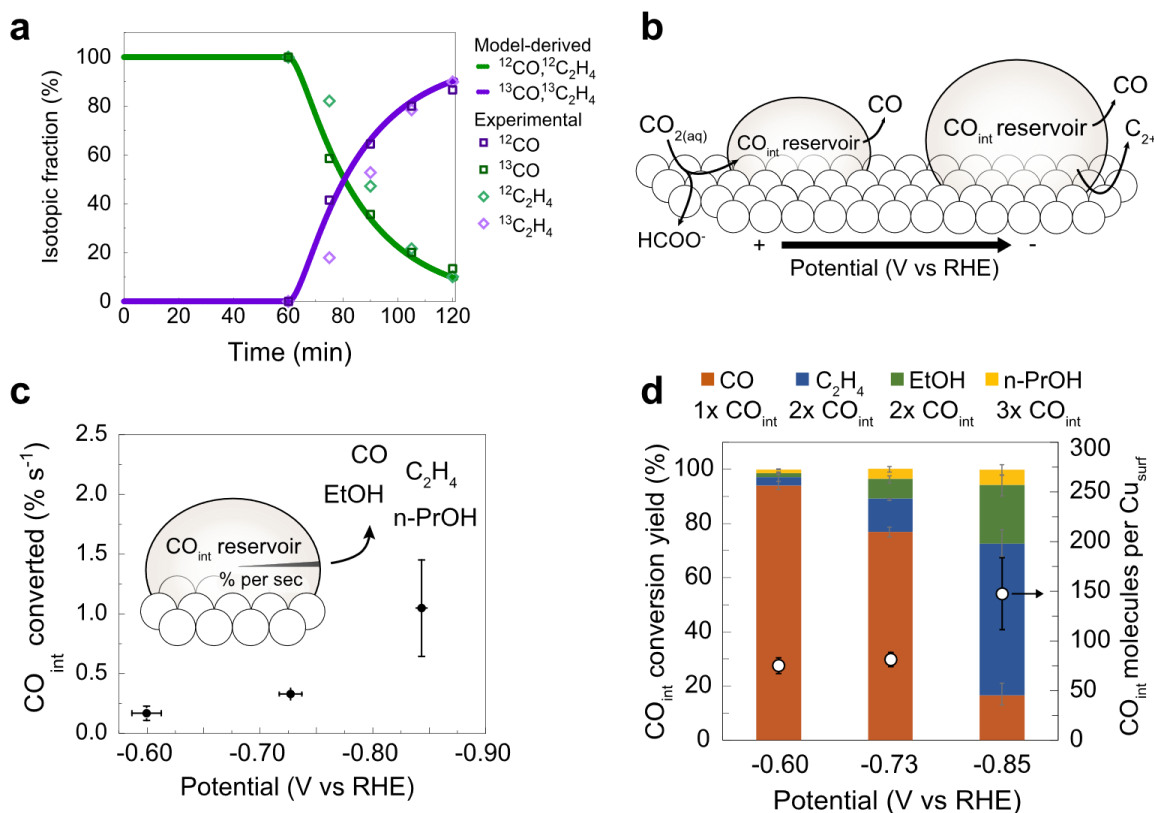


**Figure 3. Utilization of the  $\text{CO}_{\text{int}}$  reservoir on the Cu NP ensemble.** **a**, Comparison of the model-derived and experimental time-dependent change in the isotopic composition of CO and  $\text{C}_2\text{H}_4$  over the course of OSRI at -0.85 V vs RHE.  $^{12}\text{C}_2\text{H}_4$  and  $^{13}\text{C}_2\text{H}_4$  refers to the  $^{12}\text{C}$  and  $^{13}\text{C}$  fraction of all of  $\text{C}_2\text{H}_4$  isotopologues ( $^{12}\text{CH}_2\text{-}^{12}\text{CH}_2$ ,  $^{12}\text{CH}_2\text{-}^{13}\text{CH}_2$ , and  $^{13}\text{CH}_2\text{-}^{13}\text{CH}_2$ ), respectively. **b**, Schematic describing the formation and potential dependent utilization of the  $\text{CO}_{\text{int}}$  reservoir during  $\text{CO}_2\text{RR}$ . **c**, The fraction of the  $\text{CO}_{\text{int}}$  reservoir converted per second to generate  $\text{CO}_{\text{int}}$ -derived products (sum of  $\text{CO}_{\text{int}}$  consumed per second for all  $\text{CO}_{\text{int}}$ -derived products/total of  $\text{CO}_{\text{int}}$  in the reservoir) as a function of applied potential. The rate of  $\text{CO}_{\text{int}}$  consumption for each  $\text{CO}_{\text{int}}$ -derived product is derived from its partial density and the number of  $\text{CO}_{\text{int}}$  required. **d**,  $\text{CO}_{\text{int}}$  conversion yield (the number of  $\text{CO}_{\text{int}}$  consumed for one product/all  $\text{CO}_{\text{int}}$  consumed) partitioned across different  $\text{CO}_{\text{int}}$ -derived products and the  $\text{CO}_{\text{int}}$  density as a function of applied potential. The number of  $\text{CO}_{\text{int}}$  converted to each product is labeled as  $n \times \text{CO}_{\text{int}}$ , where  $n$  corresponds to the number of  $\text{CO}_{\text{int}}$  required for its formation (e.g.,  $2 \times \text{CO}_{\text{int}}$  for  $\text{C}_2\text{H}_4$ ). Error bars are one standard deviation of three independent measurements.

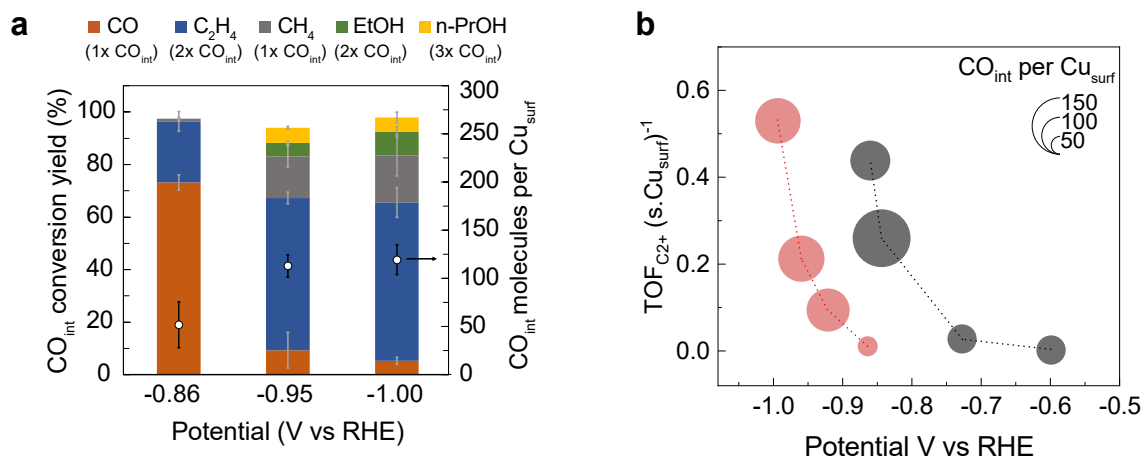


**Figure 4. Comparison between the Cu foil and the Cu NP ensemble.** **a**, CO<sub>int</sub> conversion yield (CO<sub>int</sub> consumed for each product/all CO<sub>int</sub> consumed) partitioned across different CO<sub>int</sub>-derived products and CO<sub>int</sub> density measured as a function of applied potential on the Cu foil. The number of CO<sub>int</sub> converted to each product is labeled as  $n \times \text{CO}_{\text{int}}$ , where  $n$  corresponds to the number of CO<sub>int</sub> required for its formation (e.g.,  $2 \times \text{CO}_{\text{int}}$  for C<sub>2</sub>H<sub>4</sub>). **b**, C<sub>2+</sub> turnover (dashed line) of the Cu foil and Cu NP ensemble with their CO<sub>int</sub> density (by the size of the bubble) as a function of applied potential. Bubbles are plotted to scale with respect to their diameter. Error bars are one standard deviation of three independent measurements.